Monthly Notices of the ROYAL ASTRONOMICAL SOCIETY
MNRAS 500, 3142–3150 (2021)
Advance Access publication 2020 October 23
doi:10.1093/mnras/staa3257

G0.173−0.42: an X-ray and radio magnetized filament near the galactic centre

F. Yusef-Zadeh,[1★] M. Wardle,[2] C. Heinke,[3] I. Heywood,[4,5,6] R. Arendt,[7] M. Royster,[1] W. Cotton,[8] F. Camilo[6] and J. Michail[1]

[1]CIERA, Department of Physics and Astronomy, Northwestern University, Evanston, IL 60208, USA
[2]Department of Physics and Astronomy, Research Centre for Astronomy, Astrophysics and Astrophotonics, Macquarie University, Sydney, NSW 2109, Australia
[3]Department of Physics, University of Alberta, CCIS-4-183, Edmonton, AB T6G 2E1, Canada
[4]Astrophysics, Department of Physics, University of Oxford, Keble Road, Oxford OX1 3RH, UK
[5]Department of Physics and Electronics, Rhodes University, PO Box 94, Makhanda 6140, South Africa
[6]South African Radio Astronomical Observatory, 2 Fir Street, Black River Park, Observatory, Cape Town 7925, South Africa
[7]UMBC/GSFC/CRESST 2, Code 665, NASA/GSFC, 8800 Greenbelt Rd, Greenbelt, MD 20771, USA
[8]National Radio Astronomy Observatory, Charlottesville, VA, USA

Accepted 2020 October 16. Received 2020 October 16; in original form 2020 August 28

ABSTRACT

The detection of an X-ray filament associated with the radio filament G0.173–0.42 adds to four other non-thermal radio filaments with X-ray counterparts, amongst the more than 100 elongated radio structures that have been identified as synchrotron-emitting radio filaments in the inner couple of degrees of the Galactic centre. The synchrotron mechanism has also been proposed to explain the emission from X-ray filaments. However, the origin of radio filaments and the acceleration sites of energetic particles to produce synchrotron emission in radio and X-rays remain mysterious. Using MeerKAT, VLA, *Chandra*, *WISE*, and *Spitzer*, we present structural details of G0.173–0.42 which consists of multiple radio filaments, one of which has an X-ray counterpart. A faint oblique radio filament crosses the radio and X-ray filaments. Based on the morphology, brightening of radio and X-ray intensities, and radio spectral index variation, we argue that a physical interaction is taking place between two magnetized filaments. We consider that the reconnection of the magnetic field lines at the interaction site leads to the acceleration of particles to GeV energies. We also argue against the synchrotron mechanism for the X-ray emission due to the short ∼30 yr lifetime of TeV relativistic particles. Instead, we propose that the inverse Compton scattering mechanism is more likely to explain the X-ray emission by upscattering of seed photons emitted from a 10^6 $L_\odot$ star located at the northern tip of the X-ray filament.

Key words: accretion, accretion discs – black hole physics – Galaxy: centre.

1 INTRODUCTION

More than 30 yr have elapsed since the non-thermal radio filaments (NRFs) associated with the Galactic centre radio Arc near $l \sim 0.2^\circ$ were first reported (Yusef-Zadeh, Morris & Chance 1984). These observations showed linear, magnetized features running perpendicular to the Galactic plane and since then more than 100 NRFs with similar characteristics have been discovered (Liszt 1985; Yusef-Zadeh 1986; Morris & Yusef-Zadeh 1989; Gray et al. 1991; Haynes et al. 1992; Lang, Morris & Echevarria 1999; LaRosa et al. 2004; Yusef-Zadeh, Hewitt & Cotton 2004; Law, Yusef-Zadeh & Cotton 2008; Heywood et al. 2019). The intrinsic polarization observed from these filaments shows that their magnetic fields are directed along the filaments (Yusef-Zadeh, Wardle & Parastaran 1997; Paré et al. 2019). The mechanisms responsible for accelerating particles to relativistic energies and for creating the elongated filamentary geometry are still mysterious. While several authors have examined how the filaments might arise from their interaction with molecular and ionized clouds or with mass-losing stars there is no consensus on any model (Rosner & Bodo 1996; Shore & LaRosa 1999; Bicknell & Li 2001; Yusef-Zadeh & Wardle 2019).

Chandra, *XMM*, and *NuSTAR* have detected X-ray emission from a handful of NRFs. There are four prominent radio and X-ray filaments that have been studied in detail, G359.89–0.08 (Sgr A–E), G359.54+0.18 (ripple), G359.90–0.06 (Sgr A–F), G0.13–0.11 (Sakano et al. 2003; Lu, Wang & Lang 2003; Yusef-Zadeh et al. 2005; Lu, Yuan & Lou 2008; Zhang et al. 2014; Ponti et al. 2015; Zhang et al. 2020). Unlike the long and distinct radio filaments, there are also several short, linear X-ray features that are identified in the inner 6 arcmin of Sgr A∗ (Lu et al. 2008; Muno et al. 2008; Johnson, Dong & Wang 2009). No detailed, high-resolution studies of the radio counterparts to these X-ray filaments have been published. In all previous studies, the synchrotron scenario for the X-ray emission has been proposed with the exception of G359.90–0.06 (Sgr A–F) which could be explained either by synchrotron or the inverse Compton scattering (ICS; Yusef-Zadeh et al. 2005). There are limited studies investigating the spectrum of the emission between radio and X-rays to determine the emission mechanism in radio and X-rays (Yusef-Zadeh et al. 2005). Furthermore, the origin of X-ray filaments in many studies are speculated to be traces of pulsar wind nebulae associated with pulsars (Lu et al. 2003, 2008; Zhang et al. 2020).

★ E-mail: zadeh@northwestern.edu

Here, we focus on a source discovered by *XMM*, an X-ray counterpart (Ponti et al. 2015) to the radio filament G0.173–0.42, which is also called G0.17–0.42 or S5 in Yusef-Zadeh et al. (2004). This prominent radio filament lies towards eastern boundary of a diffuse, large-scale linearly polarized plume-like structure that runs towards negative latitudes of the Galactic plane (Seiradakis et al. 1985; Yusef-Zadeh 1986; Yusef-Zadeh et al. 1990, 2004; Tsuboi et al. 1995). G0.173–0.42 consists of two parallel filaments with an extent of ∼11 arcmin oriented perpendicular to the Galactic plane (Yusef-Zadeh et al. 2004). We present X-ray observations of this filament indicating X-ray emission with an extent of ∼2 arcmin along the radio filament.

A faint oblique radio filament crosses the radio and X-ray filament. We suggest that the acceleration of relativistic particles to GeV energies occurs due to reconnection of the magnetic fields at the location where the oblique filament crosses G0.173–0.42. We argue that the flow from the acceleration site encounters a luminous mass-losing star, thus the flow wraps around the mass-losing envelope of the star before it continues to the south. In this picture, the ICS is generating X-ray emission.

2 OBSERVATIONS AND DATA REDUCTION

2.1 VLA radio observations

Radio continuum observations at 20 and 6 cm (project AY15) were carried out using the VLA in its hybrid BnC- and CnD-array configurations on 1986 October 6 and 1987 February 7, respectively. These scaled-array observations were made to determine the spectral index of G0.173–0.42. These observation were carried out in full polarization and narrow 2 × 50 MHz band. We used 3C 286 to calibrate the flux density scale, and 1748−253 to calibrate the complex gains. We used three overlapping 6 cm fields; we are focusing on one 6 cm field where X-ray emission is detected. The pointing centres at nominal frequencies at 4.80 and 1.47 GHz are α, $\delta(J2000) = 17^{h}47^{m}20\overset{s}{.}723$, $-28°59'23\overset{''}{.}362$ and α, $\delta(J2000) = 17^{h}47^{m}40\overset{s}{.}768$, $-29°01'00\overset{''}{.}806$, respectively.

2.2 MeerKAT radio observations

The Galactic centre region was observed by MeerKAT as part of its commissioning phase. The pointing used here was observed for 10.8 h on 2018 June 15, with the array pointing at α, $\delta(J2000) = 17^{h}47^{m}38\overset{s}{.}34$, $-29°06'18\overset{''}{.}95$, for an on-source time of 6.84 h. A full overview of the project will be provided by Heywood et al. (in preparation); however, a brief description of the major data processing steps are as follows. Averaging was applied to the data to reduce the native 4096 channels by a factor of 4. Basic flagging commands were applied using the `flagdata` task in CASA including bandpass edges and regions of persistent radio frequency interference. Delay and bandpass corrections were derived from observations of the primary calibrator source PKS B1934–638, which was also used to set the absolute flux scale. Time-dependent gains were derived from observations of a bright (8 Jy at 1.28 GHz) calibrator source 1827–360, which was observed for 1 min for every 10 min target scan. Gain corrections were derived iteratively with rounds of residual flagging in between. Following the application of these corrections, the target data were flagged using the TRICOLOUR package,[1] and then imaged using WSCLEAN (Offringa et al. 2014) with multiscale cleaning (Offringa & Smirnov 2017) and iterative threshold-based masking. Phase-only self-calibration solutions were derived for every 128 s of data using the `gaincal` task in CASA, and the imaging process was repeated. A Briggs (1995) robustness parameter of –1.5 was used to provide high angular resolution. The primary beam attenuation was corrected for by dividing the image by an azimuthally averaged Stokes I beam model evaluated at 1.28 GHz using the EIDOS software (Asad et al. 2019).

The spectral index α, is defined as $I_\nu \propto \nu^\alpha$ where I_ν is the intensity. Fifteen narrow channels within the broad 20 cm band were used to accurately determine the spectral index distribution. The procedure to make a spectral index image is as follows. Imaging the data in 15 sub-bands follows the application of a Gaussian taper to the visibilities of each sub-band to attempt to force common angular resolution. An inner cut to the *u,v* plane is also applied, to prevent the lowest frequencies seeing large angular scales that are not visible at higher frequencies. Each sub-image is primary beam corrected, and convolved with a circular Gaussian with an FWHM ∼ 8 arcsec. The primary beam corrected, common resolution images are stacked into a cube, which is then masked below a threshold ∼1 mJy. A linear fit for the gradient of the spectrum is made in log-frequency/log-flux space for every sightline through the masked cube for which more than 50 per cent of the frequency planes contain total intensity measurements.

2.3 *Chandra* X-ray observations

We use data from three *Chandra X-ray Observatory* observations, ObsIDs 7157 (14.9 ks), 19448 (44.5 ks), and 20111 (14.9 ks). Each observation used the Advanced CCD Imaging Spectrometer (ACIS) in the ACIS-I configuration. The data were processed using the *Chandra* X-ray Center's CIAO software package. We created images using exposure maps that divide out the instrument effective area in a variety of energy ranges, and eventually adopted 1.5–8 keV to create images (see Figs 1b, d, and 4a). We show images smoothed with a Gaussian with FWHM = 4 arcsec × 4 arcsec. The CIAO software VTPDETECT detects the filament with a false alarm probability of 2×10^{-33}. The filament is oriented at 2° clockwise of north–south in Galactic coordinates. The filament seems to extend for at least 100 arcsec ($b = -00° 26' 00''$ to $b = -00° 24' 15''$). It may extend farther to Galactic north and Galactic south.

Inspection of the merged image suggests that the filament shows three parts with different fluxes, which we designate North, South, and Centre. The Centre portion has the highest flux per unit area. A possible point source may be present at $l = 00° 10' 25\overset{''}{.}61$ $b = -00° 25' 15\overset{''}{.}99$ We extract spectra from the filament around this spot, designating it the Centre region, and from the filament on either side of it. We use extraction regions 7 arcsec in width, and with lengths 58.2, 5.7, and 41.7 arcsec, for the North, Centre, and South portions, respectively. Background regions are extracted from regions of similar width and length offset to either side of the filament by ∼10 arcsec. The total number of counts in each region is 279, 42, and 138 counts respectively. After background subtraction, we infer 260 ± 23 counts altogether can be attributed to the filament.

We fit the spectrum of the filament as a whole, and separately as three individual parts, using XSPEC version 12.10.1f. We do not combine spectra, but fit them together in XSPEC, tying parameters when appropriate (thus, all parameters are tied between epochs when fitting the spectrum of the whole filament). We fit power-law and thermal bremsstrahlung spectra, with interstellar absorption represented by the `tbabs` model assuming the `wilm` interstellar

[1] https://github.com/ska-sa/tricolour

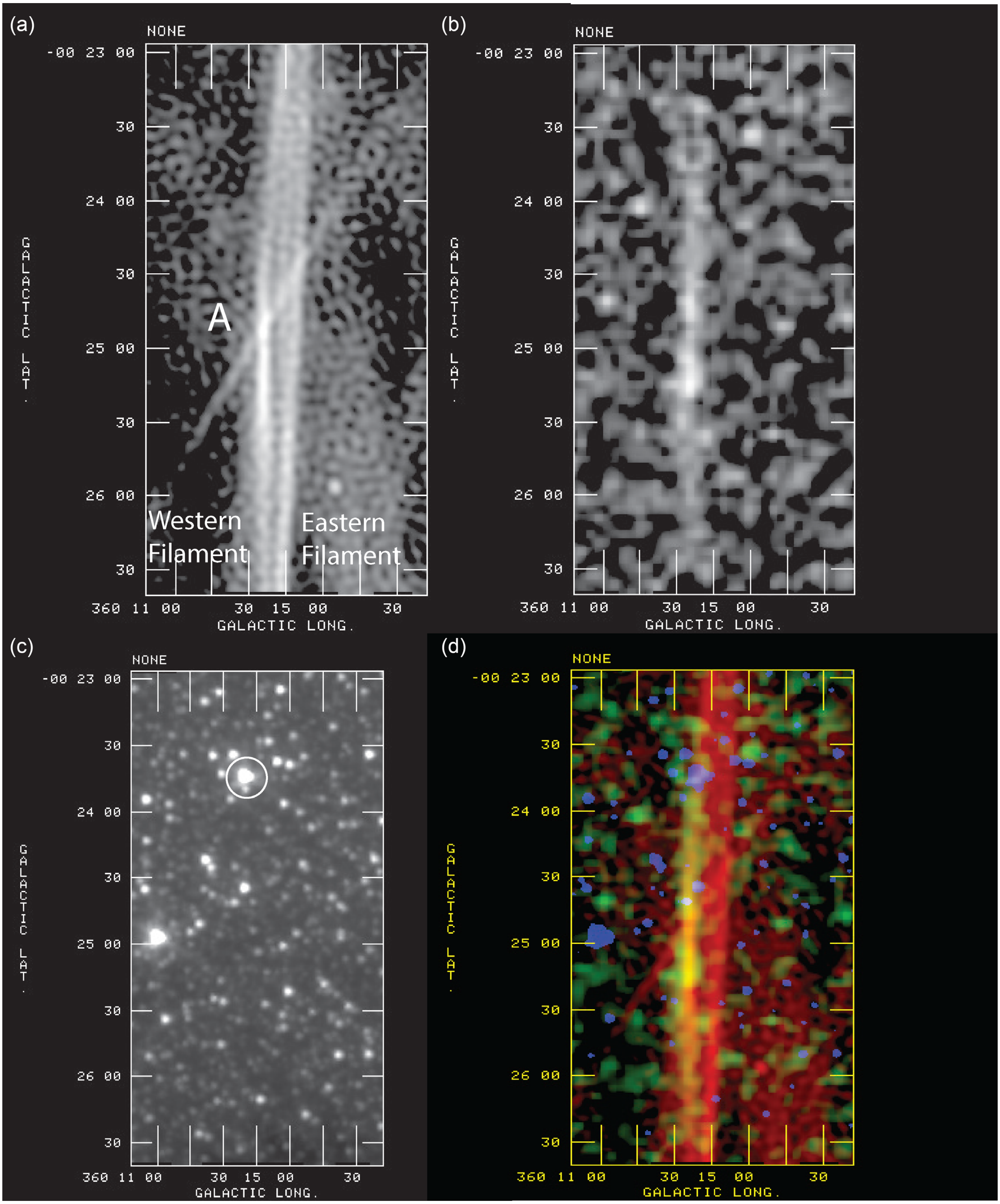

Figure 1. (*a, top left*) A grey-scale MeerKAT image at 20 cm showing an oblique filament crossing two parallel filaments at position A with a resolution of ∼4 arcsec × 4 arcsec. The eastern and western filaments are labelled. Note that diffuse radio emission surrounds the filaments. (*b, top right*) A *Chandra* X-ray image integrated between 2 and 8 keV shows a single filament coincident with the eastern radio filament but its northern extension from position A deviates to the NW in the direction away from the eastern radio filament. A circles shows the position of the bright star shown in bottom left. (*c, bottom left*) A 3.6 μm image of G0.173–0.42 taken with *Spitzer*/IRAC of *Spitzer*. A bright saturated star is located where the X-ray filament splits into two components. The bright saturated star is marked with a circle. (*d, bottom right*) A composite RGB colour image of the G0.173–0.42 filament at radio (R) and X-ray (G) superimposed on an IRAC image (B) at 3.6 μm.

abundances of Wilms et al. (2001). Due to the small number of counts, we bin the data to 1 count/bin and fit using the C-statistic.

For the full spectrum fit with a power law, we find best-fitting values of $N_H = 12^{+10}_{-6} \times 10^{22}$ cm^{-2}, photon index $\Gamma = 2.5^{+1.7}_{-1.2}$, and 2–10 keV fluxes of (unabsorbed) $2.0^{+2.5}_{-0.5} \times 10^{-13}$ erg s^{-1} cm^{-2}, or (absorbed) $1.0^{+0.2}_{-0.3} \times 10^{-13}$ erg s^{-1} cm^{-2}. Extrapolating this fit to 0.5–10 keV, we find an unabsorbed flux of 5.5×10^{-13} erg s^{-1} cm^{-2} (the high absorption and uncertainty in photon index make the intrinsic flux below 2 keV poorly constrained). Simulating 1000 fake data sets using the GOODNESS command, we find that 20 per cent give smaller test statistic values (using the Cramer–von Mises statistic), so the power-law model is acceptable.

We also test a thermal bremsstrahlung model, for which we find $N_H = 12^{+10}_{-6}$ cm^{-2}, $kT = 5^{+81}_{-3}$ keV, and unabsorbed (absorbed) 2–10 keV flux of $1.7^{+0.8}_{-0.4} \times 10^{-13}$ ($1.0^{+0.1}_{-0.2} \times 10^{-13}$) erg s^{-1} cm^{-2}. As the goodness for the bremsstrahlung fit is 24 per cent, we cannot discriminate between these two models.

Fitting the three spatial parts of the X-ray filament with a power law, we try either tying N_H and Γ between the parts, or just tying N_H. For the model with tied Γ, we find 2–10 keV unabsorbed fluxes of $1.4^{+1.6}_{-0.4} \times 10^{-13}$, $0.2^{+0.3}_{-0.1} \times 10^{-13}$, and $0.4^{+0.6}_{-0.2} \times 10^{-13}$ erg s^{-1} cm^{-2}, for the North, Centre, and South portions, respectively. If the power-law indices are freed, we find values of $\Gamma = 2.9^{+1.8}_{-1.4}$, $2.5^{+2.2}_{-2.0}$, and $1.8^{+1.9}_{-1.8}$ for the North, Centre, and South portions, respectively. We thus cannot distinguish whether there is any variation in power-law index among the three components.

2.4 2MASS, *Spitzer*, and *WISE*

In addition to radio and X-ray data, we have also examined 2MASS, *Spitzer* (IRAC and MIPS), and *WISE* images and point source catalogues of the Galactic centre (Skrutskie et al. 2006; Stolovy et al. 2006; Ramirez et al. 2008; Yusef-Zadeh et al. 2009). We employed these data to investigate the SEDs of sources that appear to be associated with filaments.

3 RESULTS

3.1 Morphology

Fig. 1 shows a close-up view of G0.173–0.42 in four different panels at 20 cm, 2–8 keV, 3.6 μm and composite three-colour image of radio, X-ray, and infrared. Fig. 1(a) shows the eastern filament with a peak flux density of ∼0.75 mJy beam^{-1} at the position A, $l = 10' 24''.3$, $b = -24' 53''.70$, where the oblique filament crosses the parallel filaments (‘A’ is defined as the intersection of the eastern filament with the oblique filament). When compared to typical surface brightness of G0.173–0.42, the intensity of the eastern filament increases by a factor of 2–3 near position A. Enhanced radio emission extends to both north and south of position A along the eastern filament. Fig. 1(b) shows the X-ray emission near position A traces enhanced radio emission along the eastern filament.

At its north end, the X-ray filament deviates to the north-east and breaks up into two filaments. This is coincident with a luminous infrared star located at $l = 10' 18''.81$, $b = 23' 44''.61$ (circled in the 3.6 μm image in Fig. 1c). The star may be the brightest member of a cluster. The candidate cluster is defined by the six stars with [3.6] < 8.5 mag that are located within 20 arcsec of the bright star. There are no other groupings as bright and dense as this within 200 arcsec, implying a $\lesssim$1 per cent chance that the candidate cluster is simply a random arrangement of stars on the line of sight. The X-ray filament deviates to the north-east and breaks up into diffuse circular-shaped structure where a stellar cluster at 3.6 μm is found. Fig. 1(d) shows a composite image revealing that the northern tip of X-ray filament has no radio counterpart but coincides with the 3.6 μm emission from the stellar cluster.

The comparison of radio and X-ray images shows that the X-ray counterpart to G0.173–0.42 lies to the east of the radio filament and the western radio filament has no X-ray counterpart (see Fig. 1c). We have not astrometrically corrected the radio and X-ray images to each other. The 90 per cent uncertainty absolute astrometry errors for *Chandra* data are 0.8 arcsec,[2] while radio interferometric astrometric errors are comparably negligible. For the VLA, the astrometric accuracy is usually down to a few percent of the beamsize. MeerKAT data give systematic errors up to an arcsecond. A shift of 1 arcsec in the X-ray or radio positions would not affect the relative alignment of the filaments which are several arcseconds across.

The X-ray filament has a length of ∼2–2.5 arcmin, far less than the radio filament that extends for ∼11 arcmin (Yusef-Zadeh et al. 2004). A second filament also runs parallel to G0.173–0.42 and the two filaments extend for a total of ∼20 arcmin (or 48 pc at the 8 kpc Galactic centre distance), as shown in Fig. 2. We note that the strongest emission in Fig. 2 arises from G0.173–0.42 where X-ray emission is detected. Lastly, the northern tip of the X-ray filament near $b \sim -23' 45''$ deviates from radio filaments that themselves bend at Galactic latitude $b \sim -23$ arcmin by about 6 arcdeg to the north-west. The high-resolution MeerKAT 20 cm image of G0.173–0.42 reveals the east and west filaments have the appearance of winding about each other and converging to the south near $b \sim -27$ arcmin. We note a third filament G0.167–0.405 crossing G0.173–0.42 at position A at an oblique angle of $-32°$. The intensity of radio emission is stronger by a factor 2–3 to the south of A when compared to the north of A. As described below, radio spectrum becomes increasingly flatter to the south of position A.

Figs 1(b) and (d) show the X-ray filament encounters the stellar cluster. It appears that the northern extension of the X-ray filament from position A splits and wraps around the brightest member of the cluster and continues as two faint parallel linear features before the emission is terminated. We consider below that there is a physical interaction of the X-ray filament with the envelope this (presumed) mass-losing luminous star. Fig. 3 shows the SED of the bright star derived from 2MASS, IRAC, MIPS *WISE* data. This star IRAC flux densities near or above the expected saturation limits. A fit to the 2MASS and *WISE* SED is also shown. Using the *WISE* data (black squares) instead of the saturated *Spitzer* IRAC data (open circles), the SED suggests about 2 mag extinction at *K* band with the corrected SED (red squares) characterized by a best-fitting stellar atmosphere model (blue stars) of $T = 9250$ K, and an absolute *K*-band magnitude of -10.9. The extinction and absolute magnitude are derived using the Galactic centre interstellar extinction law of Nishiyama et al. (2009). It may be that this source is intrinsically hot, but we cannot rule out the possibility that there is a systematic error in the temperature derivation. This error could result from using a subset of the available model atmosphere parameters or the possible presence of warm dust that adds to the stellar emission at wavelengths as short as 3.4 μm. The high temperature and the luminosity could be matched by a young massive star.

As the northern extension of the X-ray filament from position A crosses the cluster of stars, it does not follow the eastern radio filament. To demonstrate this, Fig. 4 compares the intensity in radio and X-rays along three background subtracted slices across the width of

[2]https://cxc.cfa.harvard.edu/cal/ASPECT/celmon/

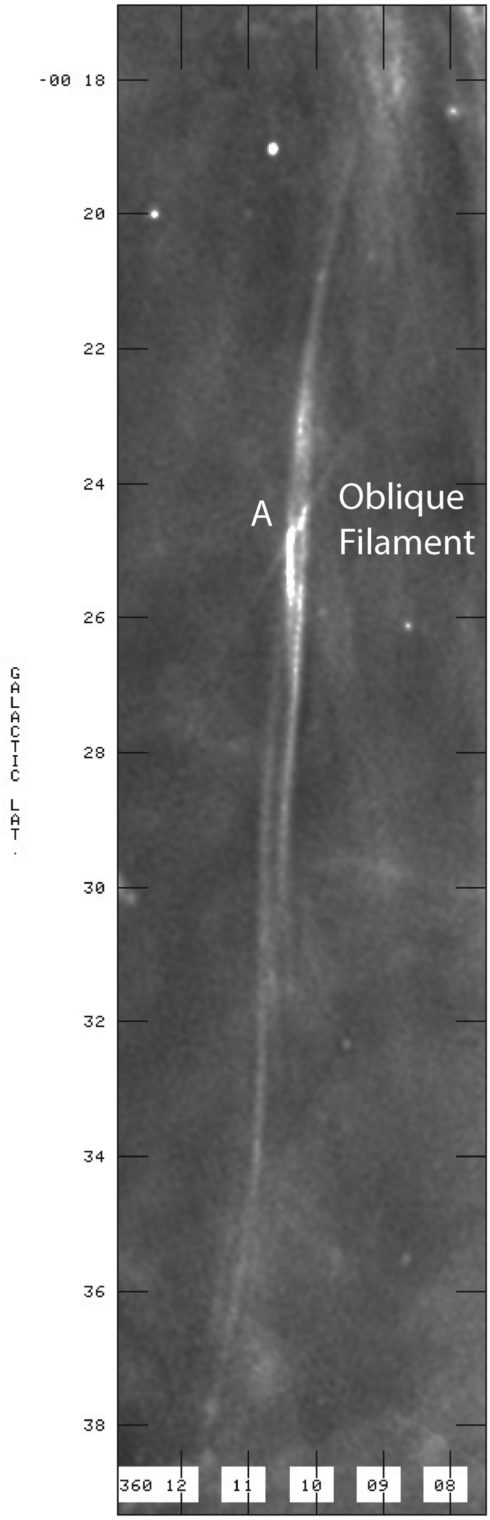

Figure 2. A 1.28 GHz image of a network of parallel filaments, the brightest portion of which includes G0.173–0.42. The range of intensity ranges between -5×10^{-5} and 3×10^{-4} Jy beam^{-1} and the spatial resolution is ~6 arcsec.

the filaments, as labelled by horizontal lines on an X-ray image. The eastern filament has an X-ray counterpart. However, the separation of the peak emission from the radio filament with respect to its X-ray counterpart increases to the north is shown in Fig. 4(b) (slice 3).

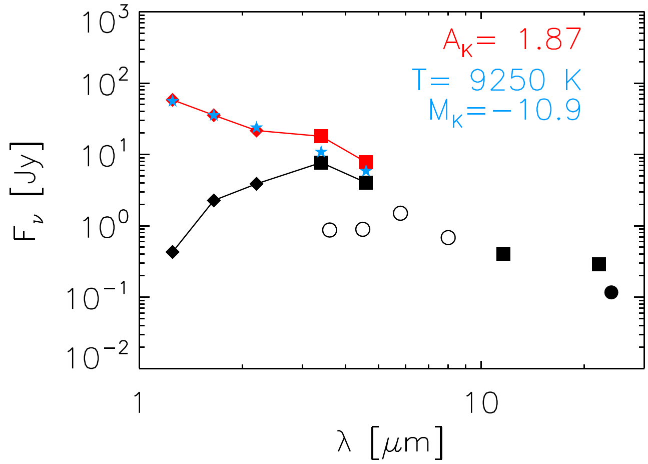

Figure 3. A spectral energy distribution (SED) of the brightest star in the cluster at the northern tip of the X-ray filament. Observed flux densities are designated by black symbols: 2MASS (diamonds), IRAC (likely affected by saturation, open circles), MIPS (filled circle), and *WISE* (squares). Red symbols indicate the extinction-corrected SED derived from a weighted fit between the 2MASS + *WISE* data and the Coelho (2014) stellar models. The fit indicates an extinction of $A_K = 1.87$ mag, and a stellar atmosphere model (blue stars) with $T = 9250$ K and an absolute *K*-band magnitude of $M_K = -10.9$.

3.2 Radio and X-ray spectrum of G0.173–0.42

The spectral index α of G0.173–0.42 is determined by measuring the flux density F_ν at 15 frequency channels within the broad 20 cm bandwidth, as shown in Fig. 5(a). G0.173–0.42 shows a north–south gradient with the steepest and flattest spectral indices of $\alpha \sim -1$ and ~ -0.2 at the northern and southern ends of the parallel filaments, respectively. The eastern and western filaments are closer together to the south, as seen on Figs 1(a) and 2, where the flattest spectral index is noted. Furthermore, the emission is strongest south of position A. It is possible that enhanced brightening and flatter spectral index are due to a new generation of energetic particles that are accelerated at the interaction site, as discussed below.

In a close-up view of the region near position A, a change in the spectral index is noted exactly where the X-ray filament lies. To illustrate this, Fig. 5(b) shows the spectral index determined from a slice cutting across the width of the filament. The eastern and western filaments show a flattening of $\alpha \sim 0.3$–0.35 with respect to background emission with steeper spectrum. The intensity of 1631.6 MHz emission from a narrow channel is also plotted in Fig. 5(b).

Fig. 6 shows a plot of radio and X-ray flux and their corresponding spectral indices. The integrated flux densities of the entire X-ray filament and the corresponding radio counterpart at 1.28 GHz are shown. The extrapolations of the radio and X-ray spectra are shown in red and blue, respectively, with dashed lines and shaded regions indicate the best-fitting spectral indices and their 90 per cent confidence intervals. The 90 per cent confidence level on the radio spectral index is computed from –1.18 ± 0.16 with a flux density of 75.5 mJy.

4 DISCUSSION

The increase in the X-ray and radio brightness of eastern filament at the location where the oblique filament crosses G0.173–0.42 suggests

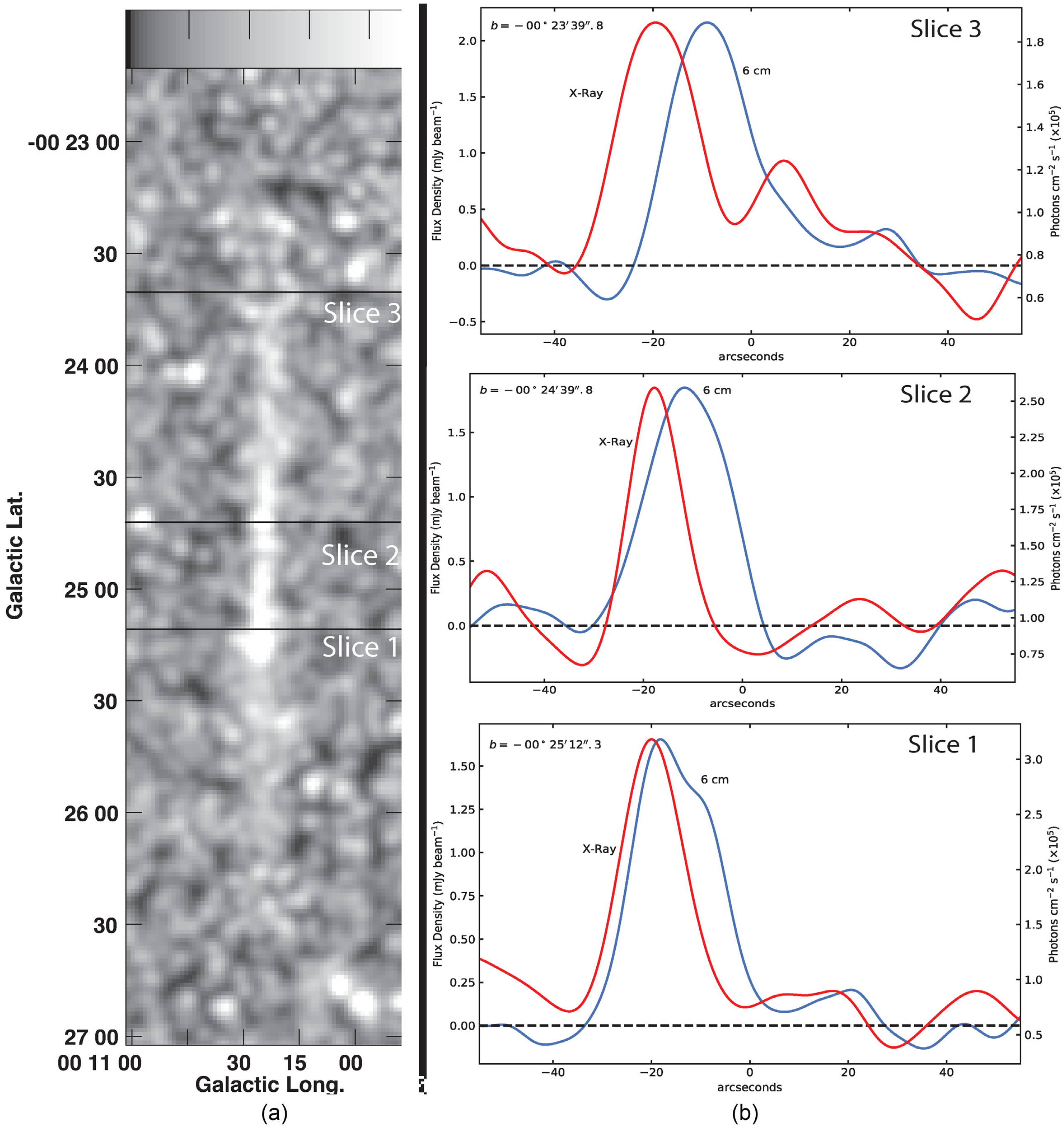

Figure 4. (*a, left*) Lines on the X-ray image show the locations of profile measurements. Only the eastern filament of G0.173–0.42 appears in X-rays. The parallel western radio filament is 10 arcsec away. (*b, right three panels*) The slice profiles show that the eastern radio filament shows an X-ray counterpart. The X-ray flux is integrated between 1.5 and 5 keV. Both radio and X-ray data are convolved to a Gaussian beam 11.95 × 8.69 arcsec with position angle (PA) 72°.55. Linear fits were used to subtract background emission from these profiles.

that the oblique filament is physically interacting with the parallel filaments. This is also supported by the observation that the oblique filament becomes fainter and wider from SE to NW as it crosses the parallel filaments.

We also note that the spectral index of radio emission is flatter to the south along the radio/X-ray filaments than to the north of the filament. This suggests that a new population of GeV electrons is injected where the oblique filament crosses the parallel filaments.

4.1 A model of X-ray and radio emission

4.1.1 *Galactic wind*

Recent detection of large-scale X-ray and synchrotron emission above and below the central molecular zone was interpreted as arising from cosmic ray driven outflow (Yusef-Zadeh & Wardle 2019). In this picture, the cosmic ray momentum and energy are mediated by the magnetic field and transferred to accelerating and heating the gas. The cosmic rays and heated gas open a channel away from the

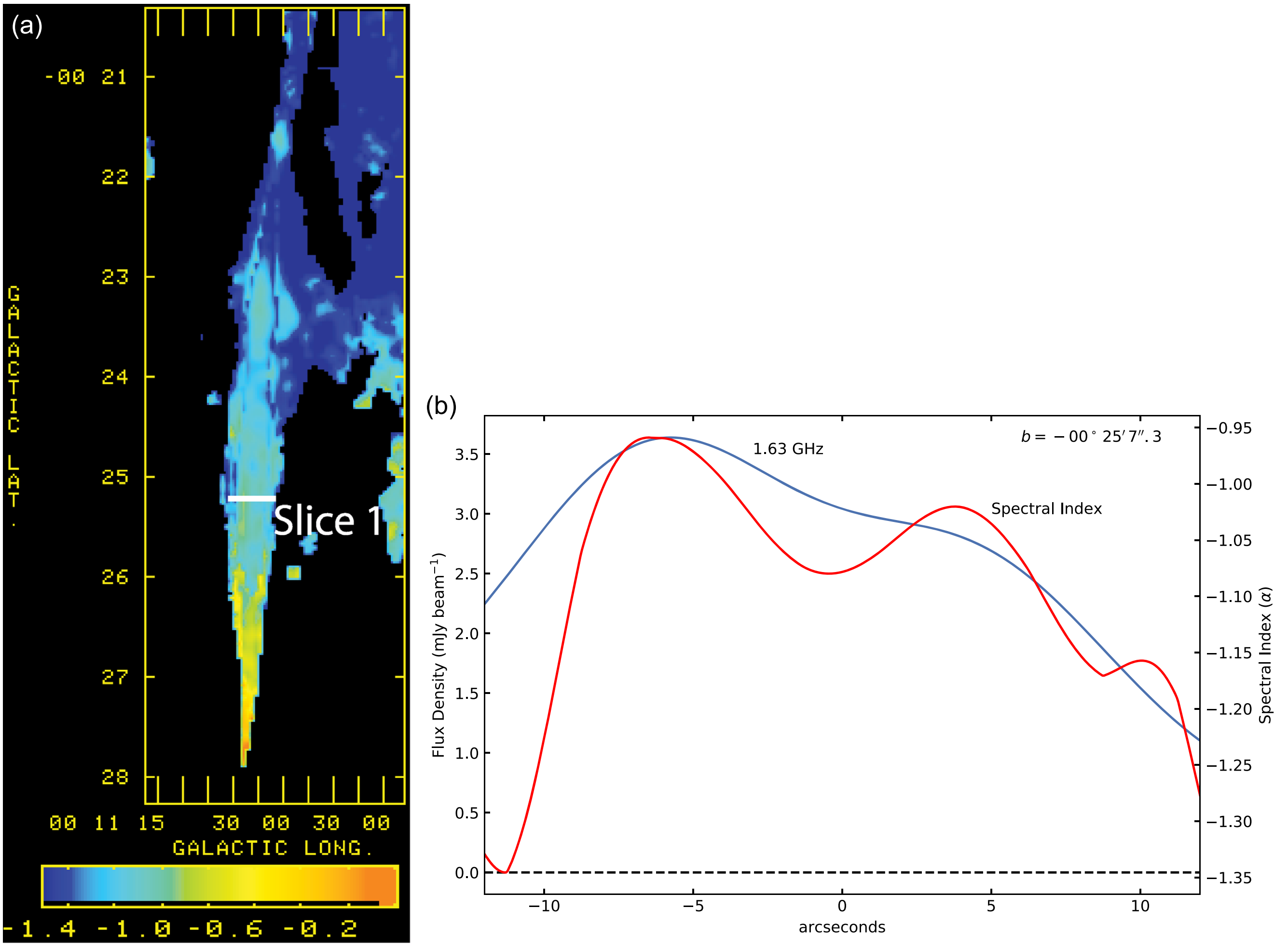

Figure 5. (*a, left*) A spectral index image based on 15 MeerKAT sub-bands within the 20 cm band between 0.8 and 1.6 GHz convolved with an 8 arcsec resolution. (*b, right*) The spectral index (red-line) determined from a slice cutting across the width of the filament, as labelled by a horizontal line segment in figure (a). The 1631.6 MHz intensity profile (blue line) of the filaments is shown for reference.

Galactic plane and expand as a Galactic wind. The interaction of this wind with any compact obstacles such as stellar wind bubbles creates the radio filaments which are analogous to cometary tails behind mass-losing stars like Mira-type stars (Martin et al. 2007). In the case of G0.173–0.42, the Galactic centre wind is expected to flow towards more negative latitudes, away from the Galactic plane. A schematic diagram of this picture is shown in Fig. 7.

4.1.2 *Interaction of two filaments: magnetic reconnection*

Because of the morphological evidence of the physical interaction of the oblique and north–south NRFs, it is plausible that reconnection of their magnetic field lines generates a new population of energetic particles. This population is responsible not only for the sudden increase in radio emission but also X-ray emission from G0.173–0.42 at point A.

The 1.2 GHz radio continuum emission along the eastern filament brightens to the south of point A, where it is crossed by the oblique filament. This brightening is accompanied by the flattening of the spectrum, from $\sim\nu^{-1.4}$ to north of A, to $\nu^{-0.5}$ to the south. The profile of the oblique filament becomes more diffuse and complex as it crosses the vertical filament at A. Together, these changes point to a physical interaction of the filaments at position A suggestive of the acceleration of electrons at A. One possible form of this interaction is magnetic reconnection. In this case, some of the dissipated magnetic energy is transferred to a new population of relativistic electrons. To estimate the available magnetic power, we adopt a nominal field strength $B = 100\,\mu$G (Yusef-Zadeh et al. 2005; Yusef-Zadeh & Wardle 2019), reconnection speed $\upsilon = 20\,\mathrm{km\,s^{-1}}$, and cross-sectional area $A = (0.2\ \mathrm{pc})^2$. Then the reconnection gives a power, $L_r \sim \upsilon_A\, A\, B^2/8\pi \approx 3\times10^{32}\,\mathrm{erg\,s^{-1}}$ and the lifetime of the interaction is of order the filament width, 0.2 pc, divided by the reconnection speed, 20 km s^{-1}, i.e. $\sim 10^4$ yr.

The energy of the electrons dominating the emission at 1.2 GHz is ∼0.9 GeV, and their synchrotron lifetime is ∼0.9 Myr. The enhanced radio emission associated with this population extends ≈2 pc to the south. If this were determined by the synchrotron lifetime, then their propagation speed would only be ∼2 km s^{-1}, an order of magnitude below the ∼20 km s^{-1} cosmic ray streaming speed that is commonly inferred elsewhere. Instead, the spatial extent of the enhanced continuum emission is likely set by the time elapsed since the interaction between the filaments commenced. If the total interaction time-scale between the filament is 10^4 yr, as estimated above, then the age of the electrons must be less than this, suggesting a propagation speed in excess of 200 km s^{-1}. This is far higher than the speeds associated with cosmic ray streaming.

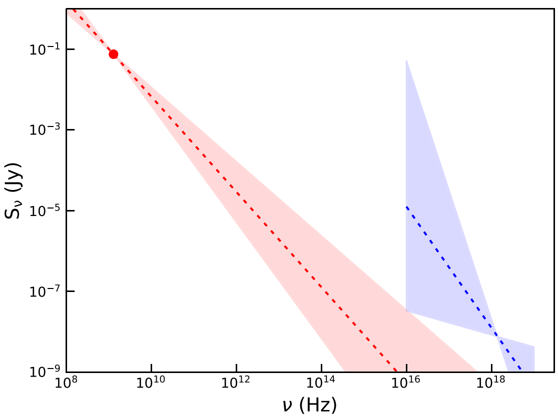

Figure 6. The integrated flux densities of the entire X-ray filament and the corresponding radio counterpart at 1.28 GHz. The extrapolations of the radio and X-ray spectra are shown in red and blue, respectively, with dashed lines and shaded regions indicate the best-fitting spectral indices and their 90 per cent confidence intervals. The 90 per cent confidence level on the radio spectral index is computed from –1.18 ± 0.16 with a flux density of 75.5 mJy. Took them from the text. The X-ray photon index $\Gamma = 2.5^{+1.7}_{-1.2}$ with a 2–10 keV fluxes (unabsorbed) $2.0^{+2.5}_{-0.5} \times 10^{-13}$ erg s^{-1} are used to determine the best-fitting spectral index to X-ray data.

This is consistent with a model in which non-thermal filaments at the Galactic centre are a result of a large-scale cosmic ray driven wind (Yusef-Zadeh & Wardle 2019). In this picture, a net flow of plasma away from the galactic plane at hundreds of km s^{-1} is driven by the extreme cosmic ray pressure in the central 150 pc of the Galaxy (Oka et al. 2019). The non-thermal filaments are magnetized streamers created by the wrapping of the wind's magnetic field around an obstacle to the flow, by analogy with the magnetized ion tails of comets embedded in the solar wind. The relativistic electrons injected by reconnection are advected by this flow, and the time to be transported from the injection point A to the southern tip of the radio-brightened portion for the filament is a few thousand years, consistent with the expected interval since the interaction between the two filaments began.

4.1.3 *Enhanced X-ray emission: ICS*

We now turn to the origin of the X-ray emission. This is unlikely to be synchrotron emission for three reasons. First, the distribution does not match that of the brighter, flat spectrum radio emission, but extends a couple of pc to the north and south of the injection point A. Secondly, the lifetime of the ~30 TeV electrons that would radiate in the keV range via synchrotron emission would be only 30 yr, implying that their propagation speed to the north and south from the injection point would need to exceed 0.2 c. Thirdly, the X-ray flux is too high to be consistent with the spectral index at radio wavelengths. To support this, we determined the integrated 1.28 GHz flux with a beam size of 8 arcsec × 8 arcsec over the area covering the X-ray filament, ~25.2 arcsec × 167.5 arcsec, giving 75.5 ± 13.2 mJy. The spectral index in the 20 cm band is estimated to be –1.18 ± 0.16 and is shown in Fig. 6.

Instead an ICS scenario seems preferred, in which the X-ray emission is created by the upscattering of seed photons contributed by the bright stellar source located at the northern tip of the X-ray emission. The ICS flux F_{ν_x} at frequency ν_x is given by

$$\nu_x F_{\nu_x} \approx 0.5\, \frac{\nu_1 U_{\nu_1}}{U_B}\, \nu_0 F_{\nu_0}, \qquad (1)$$

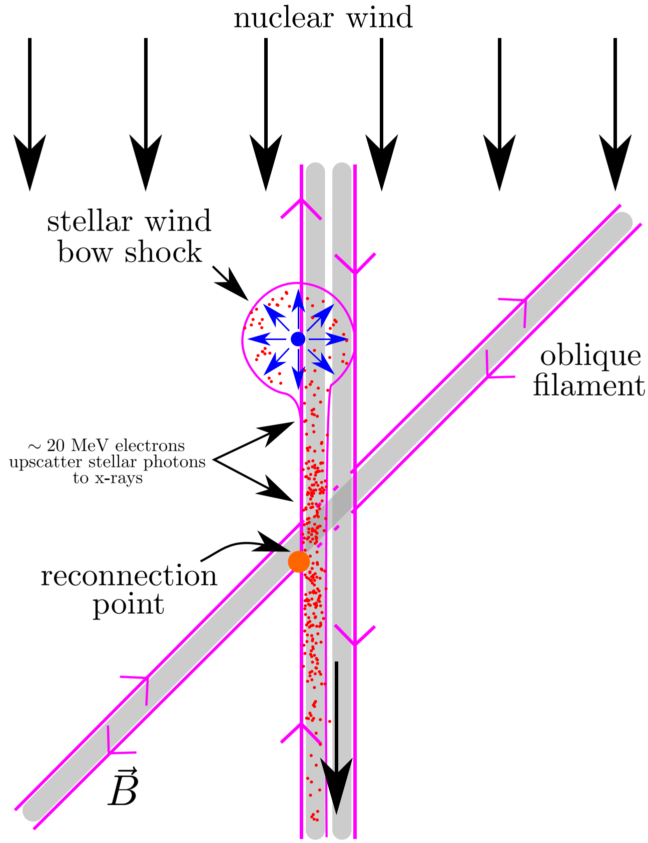

Figure 7. A schematic diagram of an oblique filament crossing two parallel filaments, producing a new population of relativistic particles. Cosmic ray particles from the nuclear wind and the reconnection point interact in two locations with the seed photons of a luminous mass-losing star and produce X-ray emission due to ICS, as shown in red.

$\nu 1\, U_{\nu_1}$ is the energy density of the seed photons at the peak of the stellar spectrum at frequency ν_1, U_B is the energy density magnetic field, and ν_0 is the characteristic frequency of the synchrotron emission of electrons with Lorentz factor $\gamma \sim (\nu_X/\nu_1)^{1/2}$.

Adopting a stellar luminosity $L_* \approx 1 \times 10^6\,\mathrm{L}_\odot$, with an SED peaking at $\nu_1 = 0.5\,\mu$m, typical of a young massive star, then upscattering to $h\nu_X \approx 5$ keV is achieved by electrons in the low-energy tail with Lorentz factors ≈50. The energy density at distance d from the star is $U_\nu = L_\nu/(4\pi c d^2)$. Adopting a synchrotron flux of 0.1 Jy at 1.2 GHz and a $\nu^{-1.4}$ spectrum then $\nu F_\nu \propto \nu^{-0.4}$ and for our nominal field strength of 100 μG (Yusef-Zadeh et al. 2005; Yusef-Zadeh & Wardle 2019), this yields 0.5–10 keV X-ray flux over the extent of the X-ray filament of about 2 × 10^{-13} erg cm^{-2} s^{-1}, consistent with the observed X-ray flux. Reducing the adopted magnetic field strength to 50 μG increases the X-ray flux to 8 × 10^{-13} erg cm^{-2} s^{-1}.

In this scenario, the X-ray emission traces ~20 MeV electrons that are injected at (a) the stellar bow shock and (b) the reconnection point where the oblique filament crosses the north–south filament at point A (see Fig. 6). In both cases, the injected particles are carried southwards by the large-scale nuclear wind from the inner 100 pc of the Galaxy. ICS of the additional electrons injected at A offsets the $1/r^2$ decline of the seed photon density with distance from the star and maintains a relatively uniform surface brightness along the north–south filament.

4.2 Summary

We have presented a moderate-resolution study of the radio structure and spectral index of G0.173–0.42 which consists of two parallel filaments and an oblique filament G0.167–0.405 crossing the parallel filaments. A small portion of one of the two parallel filaments has an X-ray counterpart. Noting the variation in spectral index, sudden brightening and asymmetry of radio and X-ray emission, we argued for an interaction of the oblique filament with one of the two parallel filaments and suggested injection of a new population of relativistic particles due to magnetic field reconnection. The presence of a Galactic centre wind produces lopsided profiles through its tendency to push particles away from the injection point. We suggested that the ICS mechanism is more likely to explain the X-ray emission by upscattering of seed photons emitted from a 10^6 $L_\odot$ star located at the northern tip of the X-ray filament. We argued against the synchrotron mechanism for the X-ray emission due to the short ∼30 yr lifetime of TeV relativistic particles.

ACKNOWLEDGEMENTS

This work is partially supported by the grant AST-0807400 from the National Science Foundation. The MeerKAT telescope is operated by the South African Radio Astronomy Observatory, which is a facility of the National Research Foundation, an agency of the Department of Science and Innovation. IH acknowledges support from the UK Science and Technology Facilities Council (ST/N000919/1), the Oxford Hintze Centre for Astrophysical Surveys which is funded through generous support from the Hintze Family Charitable Foundation, and a visiting Professorship from SARAO. We acknowledge use of the Inter-University Institute for Data Intensive Astronomy (IDIA) data intensive research cloud for data processing. IDIA is a South African university partnership involving the University of Cape Town, the University of Pretoria, and the University of the Western Cape. MW thanks the Cherrybrook Research Institute for hospitality. The authors acknowledge the Centre for High Performance Computing (CHPC), South Africa, for providing computational resources to this research project.

DATA AVAILABILITY

All the data including X-ray, radio, and IR data that we used here are available online and are not proprietary. We have reduced and calibrated these data and are available if requested.

REFERENCES

Asad K. M. B. et al., 2019, preprint (arXiv:1904.07155)
Bicknell G. V., Li J., 2001, ApJ, 548, L69
Briggs D. S., 1995, American Astronomical Society 187th AAS Meeting, Bulletin of the American Astronomical Society, Vol. 27, p. 1444
Coelho P. R. T., 2014, MNRAS, 440, 1027
Gray A. D., Cram L. E., Ekers R. D., Goss W. M., 1991, Nature, 353, 237
Haynes R. F., Stewart R. T., Gray A. D., Reich W., Reich P., Mebold U., 1992, A&A, 264, 500
Heywood I. et al., 2019, Nature, 573, 235
Johnson S. P., Dong H., Wang Q. D., 2009, MNRAS, 399, 1429
Lang C. C., Morris M., Echevarria L., 1999, ApJ, 526, 727
LaRosa T. N., Nord M. E., Lazio T. J. W., Kassim N. E., 2004, ApJ, 607, 302
Law C. J., Yusef-Zadeh F., Cotton W. D., 2008, ApJS, 177, 515
Liszt H. S., 1985, ApJ, 293, L65
Lu F. J., Wang Q. D., Lang C. C., 2003, AJ, 126, 319
Lu F. J., Yuan T. T., Lou Y.-Q., 2008, ApJ, 673, 915
Martin D. C. et al., 2007, Nature, 448, 780
Morris M., Yusef-Zadeh F., 1989, ApJ, 343, 703
Muno M. P., Baganoff F. K., Brandt W. N., Morris M. R., Starck J.-L., 2008, ApJ, 673, 251
Nishiyama S. et al., 2009, ApJ, 690, 1648
Offringa A. R., Smirnov O., 2017, MNRAS, 471, 301
Offringa A. R. et al., 2014, MNRAS, 444, 606
Oka T., Geballe T. R., Goto M., Usuda T., Benjamin, McCall J., Indriolo N., 2019, ApJ, 883, 54
Paré D. M., Lang C. C., Morris M. R., Moore H., Mao S. A., 2019, ApJ, 884, 170
Ponti G. et al., 2015, MNRAS, 453, 172
Ramirez S. V., Arendt R. G., Sellgren K., Stolovy S. R., Cotera A., Smith H. A., Yusef-Zadeh F., 2008, ApJS, 175, 147
Rosner R., Bodo G., 1996, ApJ, 470, L49
Sakano M., Warwick R. S., Decourchelle A., Predehl P., 2003, MNRAS, 340, 747
Seiradakis J. H., Lasenby A. N., Yusef-Zadeh F., Wielebinski R., Klein U., 1985, Nature, 317, 697
Shore S. N., LaRosa T. N., 1999, ApJ, 521, 587
Skrutskie M. F. et al., 2006, AJ, 131, 1163
Stolovy S. et al., 2006, J. Phys. Conf. Ser., 54, 176
Tsuboi M., Kawabata T., Kasuga T., Handa T., Kato T., 1995, PASJ, 47, 829
Wilms J., Reynolds C. S., Begelman M. C., Reeves J., Molendi S., Staubert R., Kendziorra E., 2001, MNRAS, 328, L27
Yusef-Zadeh F., 1986, PhD thesis, Columbia University
Yusef-Zadeh F., Wardle M., 2019, MNRAS, 490, L1
Yusef-Zadeh F., Morris M., Chance D., 1984, Nature, 310, 557
Yusef-Zadeh F., Morris M., Lasenby A. N., Seiradakis J. H., Wielebinski R., 1990, in Beck R., Kronberg P. P., Wielebinski R., eds, Proc. IAU Symp. 140, Galactic and Intergalactic Magnetic Fields. Kluwer Academic Publishers, Dordrecht, p. 373
Yusef-Zadeh F., Wardle M., Parastaran P., 1997, ApJ, 475, L119
Yusef-Zadeh F., Hewitt J. W., Cotton W., 2004, ApJS, 155, 421
Yusef-Zadeh F., Wardle M., Muno M., Law C., Pound M., 2005, Adv. Space Res., 35, 1074
Yusef-Zadeh F. et al., 2009, ApJ, 702, 178
Zhang S. et al., 2014, ApJ, 784, 6
Zhang S. et al., 2020, ApJ, 893, 3

This paper has been typeset from a TEX/LATEX file prepared by the author.